A Physical Model of Nonstationary Blur in Ultrasound Imaging

Adrien Besson, *Student Member, IEEE*, Lucien Roquette, Dimitris Perdios, *Student Member, IEEE*, Matthieu Simeoni, *Student Member, IEEE*, Marcel Arditi, *Senior Member, IEEE*, Paul Hurley, Yves Wiaux, and Jean-Philippe Thiran, *Senior Member, IEEE*

***Abstract*—While restoration methods have been extensively studied in ultrasound (US) imaging, only few recent works have focused on modeling and understanding the blur from a physical point of view even in simple configurations, such as lossless homogeneous media. Despite a highly nonstationary blur due to diffraction effects, many techniques rely on simplistic approximations based on shift-invariant models or sectional methods and their efficiency has not been demonstrated for plane-wave (PW) and diverging-wave (DW) imaging. In this paper, we first propose a physical model of nonstationary blur in the context of PW and DW imaging. The blur operation is expressed as a composition of a U.S. propagation operator and a delay-and-sum operator, each of which has derived in previous works. We show that such a composition leads to a standard model of nonstationary blur as a Fredholm integral of the first kind. Second, we describe an approximation of the blur in the discrete domain based on the above decomposition coupled with an appropriate discretization of the latent element-raw-data space. We show theoretically and empirically that its evaluation, using such an approximation, scales linearly instead of quadratically with respect to the grid size, better than shift-invariant approaches. Through simulations and *in vivo* experimental data, we demonstrate that using the proposed model in the context of maximum-a-posteriori image restoration results in a higher image quality than using state-of-the-art shift-invariant models.**

***Index Terms*—Nonstationary blur, restoration, ultrasound imaging.**

Manuscript received April 4, 2018; revised August 3, 2018, November 27, 2018, January 8, 2019, and January 20, 2019; accepted February 3, 2019. Date of publication February 6, 2019; date of current version August 2, 2019. This work was supported in part by the UltrasoundToGo RTD Project under Grant 20NA21_145911, evaluated by the Swiss National Science Foundation and funded by Nano-Tera.ch with Swiss Confederation financing, and in part by the U.K. Engineering and Physical Sciences Research Council under Grant EP/M019306/1. The associate editor coordinating the review of this manuscript and approving it for publication was Prof. Alessandro Foi. *(Corresponding author: Adrien Besson.)*

A. Besson, D. Perdios, and M. Arditi are with the Signal Processing Laboratory 5 (LTS5), Ecole Polytechnique Fédérale de Lausanne, CH-1015 Lausanne, Switzerland (e-mail: adrien.besson@epfl.ch; dimitris.perdios@epfl.ch; marcel.arditi@epfl.ch).

L. Roquette and P. Hurley are with the Cognitive Computing Department, IBM Research, 8803 Ruschlikon, Switzerland (e-mail: lucien.roquette@epfl.ch; pah@zurich.ibm.com).

M. Simeoni is with the Cognitive Computing Department, IBM Research, 8803 Ruschlikon, Switzerland, and also with the Laboratoire de Communications Audiovisuelles, Ecole Polytechnique Fédérale de Lausanne, CH-1015 Lausanne, Switzerland (e-mail: matthieu.simeoni@ibm.ch).

Y. Wiaux is with the Institute of Sensors, Signals and Systems, Heriot-Watt University, Edinburgh EH14 4AS, U.K. (e-mail: y.wiaux@hw.ac.uk).

J.-Ph. Thiran is with the Signal Processing Laboratory 5 (LTS5), Ecole Polytechnique Fédérale de Lausanne, CH-1015 Lausanne, Switzerland, and also with the Department of Radiology, University Hospital Center (CHUV) and University of Lausanne (UNIL) CH-1011 Lausanne, Switzerland (e-mail: jp.thiran@epfl.ch).

This paper has supplementary downloadable material available at http://ieeexplore.ieee.org, provided by the authors. This includes an additional figure illustrating the results of the numerical experiment on the PICMUS dataset. This material is 846 MB in size.

Digital Object Identifier 10.1109/TCI.2019.2897951

I. Introduction

ULTRASOUND (US) imaging is a widely used medical imaging modality due to its non-invasiveness, relative low-cost and real time capability. By appropriately placing a US probe, usually composed of an array of piezoelectric transducer elements, a medical doctor is able to visualize cross-section images of regions of interest in the body.

The US imaging process exploits the transducer elements for both transmitting acoustic pulses and recording the response of the medium to these pulses as echo signals. The set of these signals is related to the spatial distribution of variations in acoustic impedance, i.e. in medium density and sound velocity, denoted as the tissue reflectivity function (TRF), by a US propagation operator. Due to the finite aperture of the probe and the bandpass properties of each transducer element, retrieving the TRF from the echo signals is an ill-posed problem. In standard US imaging, the delay-and-sum (DAS) operator is used as an approximate adjoint of the propagation operator. Such an approximation leads to a radio-frequency (RF) image, a blurred estimate of the TRF. The point spread function (PSF) is introduced to relate these quantities. Because of the wave propagation and diffraction effects in the medium, the blur is spatially varying, as can be seen in Fig. 1.

While the principles of the propagation of US waves in a homogeneous and lossless medium have been known for more than a century, only few recent studies have focused on understanding the PSF from a physical point of view [1], [2]. In the vast majority of studies, the PSF is estimated in a preliminary step either through *in vitro* measurements or by simulation [3]–[7]. Other approaches estimate directly the PSF on the RF image in a first stage and then use the estimated PSF to perform the restoration. In these cases, the PSF estimation is typically performed using homomorphic filtering of the cepstrum [8]–[10], generalized homomorphic filtering [11], [12], inverse filtering [13]–[17] and power spectrum equalization [18]. Alternatively, blind deconvolution methods, where the PSF and the TRF

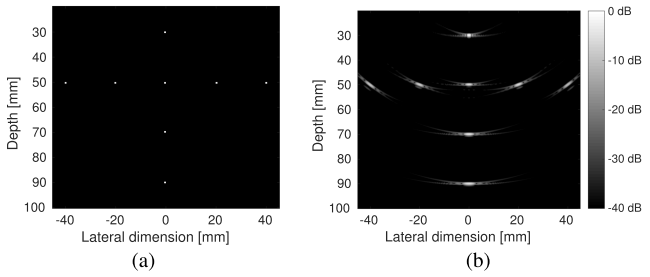

Fig. 1. An example of a TRF (a) and the corresponding demodulated RF image (b) obtained with the DAS operator. We clearly see the spatially varying blur induced by classical US imaging system.

are jointly estimated, have been very popular recently with the development of regularization approaches. Such methods involve either parametric [19]–[21] or non-parametric [6], [22] models of the PSF.

In addition, evaluating the non-stationary blur, assumed linear, for image restoration purpose requires to perform matrix-vector products with large matrices (around 10^{10} coefficients for 2D US images) which is very challenging with standard numerical tools.

Such a problem is standard in shift-variant deblurring and many simplification strategies have been developed in the literature. Most of them are based on the assumption that non-stationary blur can be approximated by a relatively low number of basis filters. The evaluation of the blur is then performed as a weighted sum of convolutions with the basis filters [23]. (See [24] for an exhaustive description of such methods.)

In this group of techniques, sectional methods are probably the most popular ones [25]–[29]. In such approaches, the image is divided into sub-regions where the blur is considered stationary. Then, by appropriately masking the image, shift-invariant convolutions are applied in each sub-region independently forming different sub-images that are interpolated to form the blurred image. In this case, the basis filters correspond to blur kernels. Other techniques rely on low-rank approximations of the non-stationary blur where the basis filters are the corresponding eigenvectors [24], [30], [31].

Alternatively, several recent works propose to approximate the blur with an operator that has desirable properties, e.g. diagonalizability [32] or sparsity [33], [34] in given frames.

In the context of US imaging, the most advanced techniques achieve shift-variant restoration using sectional methods [11], [29], [35] which assume lateral stationarity of the blur, suited to the case of US imaging with focused waves. These approaches are evidently not valid in plane-wave (PW) and diverging-wave (DW) imaging where the diffraction effects are substantial, as displayed in Fig. 1.

In this work, we propose the following contributions:

- We describe a novel model of non-stationary blur in US imaging with PW and DW insonifications. We show that the model can be expressed as a composition of a US propagation operator [2], [36] and a DAS operator, each of which described in previous works [37], [38]. We also relate the proposed model with the one detailed by Roquette *et al.* [1].
- We propose an approximation of non-stationary blur for image restoration which exploits the above introduced decomposition coupled with an appropriate discretization of the latent element-raw-data space. We demonstrate that its evaluation, based on efficient formulations of the discrete operators [37], scales linearly rather than quadratically, with the size of the grid, in a better way than shift-invariant blur evaluation methods.
- We show an example application of US image restoration. More precisely, we use the proposed model in a maximum-a-posteriori (MAP) estimation algorithm, with a generalized Gaussian distribution (GGD) prior for the TRF [6], [12]. We test the method on an extensive number of experiments, namely a numerical phantom of point reflectors, a numerical calibration phantom and two *in vivo* carotids, for both DW and PW imaging. We demonstrate that the proposed restoration method leads to an improvement of the lateral and axial resolution, compared to methods based on state-of-the-art shift-invariant models of the blur, on both the point-reflector and the calibration phantoms and provides a higher contrast and visual quality on *in vivo* carotid images. All the experiments presented in the paper are reproducible and supporting code is available at https://github.com/LTS5/us-non-stationary-deconv.

The remainder of the paper is organized as follows. Section II introduces the model of non-stationary blur and Section III describes the proposed evaluation strategy in the discrete domain. Experimental settings are described in Section IV and results are reported and discussed in Section V. Concluding remarks are given in Section VI.

II. Mathematical Modeling of the Non-Stationary Blur at the Continuous Level

In this section, we describe a mathematical model of the non-stationary blur and propose formulations of the associated operators at the continuous level.

A. Notation

In the paper, we denote by $L_2(\Omega)$ the Hilbert space of the square integrable functions which take values in a space Ω. In addition, for $f, g \in L_2(\Omega)$, we denote their inner product as $\langle f, g \rangle_{L_2(\Omega)}$ and their convolution as $f * g$. The adjoint of a linear operator $\mathcal{H} : L_2(\Omega_1) \to L_2(\Omega_2)$ is given by $\mathcal{H}^\dagger : L_2(\Omega_2) \to L_2(\Omega_1)$. (See Chapter 2 of [39] for a review on linear operators.)

The Hermitian transpose of a matrix $\boldsymbol{X} \in \mathbb{R}^{M \times N}$ is denoted by $\boldsymbol{X}^\dagger$ and the transpose by $\boldsymbol{X}^\top$. $\boldsymbol{X}_{\bullet J}$ is the sub-matrix formed by the restriction of $\boldsymbol{X}$ to the columns indexed by the set $J \subset \{1, \ldots, n\}$. The Hadamard product between $\boldsymbol{X}$ and $\boldsymbol{Y}$ is denoted by $\boldsymbol{X} \circ \boldsymbol{Y}$.

Given a vector $\boldsymbol{a} \in \mathbb{R}^N$ and a positive real $p \in \mathbb{R}_+$, we define its p-norm as $\|\boldsymbol{a}\|_p = \sqrt[p]{\sum_{i=1}^N |a_i|^p}$.

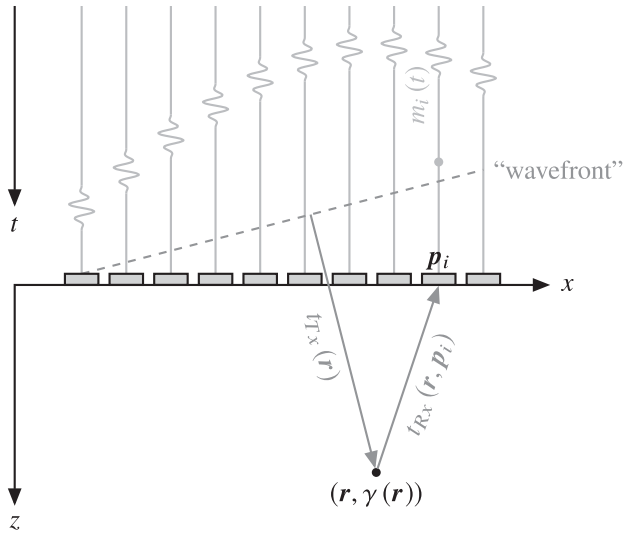

Fig. 2. Standard 2D US imaging configuration (adapted from [37]).

B. Proposed Model of the Non-Stationary Blur in Ultrasound Imaging

In a standard 2D pulse-echo US imaging configuration, described in Fig. 2, an array of transducer elements is used to propagate an acoustic wave in a medium $\Omega \subset \mathbb{R}^2$ which contains inhomogeneities as local fluctuations in acoustic impedance, defining the TRF $\gamma \in L_2(\Omega)$ [11], [37], [40]. Depending on the desired transmit wavefront, e.g. PW, DW, focused-wave or synthetic-aperture approaches, each transducer element starts to transmit after a given delay defined by an inter-element delay profile.

In a receive phase, a set of transducer elements, located at $\{\boldsymbol{p}_i\}_{i=1}^{N_{el}}$, $\boldsymbol{p}_i \in \mathbb{R}^2$, detect echo signals $m_i(t)$, $t \in [0, T]$, defining the following measurements

$$m(t) := [m_1(t), \ldots, m_{N_{el}}(t)] \in L_2([0,T])^{N_{el}}, \quad (1)$$

where $L_2([0,T])^{N_{el}} := L_2([0,T]) \times \cdots \times L_2([0,T])$.

1) Ultrasound Propagation Operator: The measurements $m(t)$ are related to the TRF γ by the propagation of the US wave during the time interval $[0, T]$. It can be demonstrated using the first order Born approximation that a linear operator $\mathcal{H} : \gamma \mapsto m$, called the US propagation operator, relates the TRF to the measurements [36]–[38]. The proposed physical modeling of wave propagation is based on the pulse-echo spatio-temporal impulse response model introduced by Stepanishen [41]. Furthermore, the effect of the transducer element surface is approximated by a directivity function using a far-field assumption [42]. Under this approximation, we can express the element-raw data received by the i-th transducer element as

$$m_i(t) = \int_{\boldsymbol{r}\in\Omega} o(\boldsymbol{p}_i, \boldsymbol{r})\, v_{pe}(t - \tau(\boldsymbol{r}, \boldsymbol{p}_i))\, \gamma(\boldsymbol{r})\, d\boldsymbol{r}, \quad (2)$$

where $o(\boldsymbol{p}_i, \boldsymbol{r})$ accounts for the spatial directivity and decay of the reflected wave and $v_{pe}(t)$ is the pulse-echo waveform [43] which depends on the transducer impulse response and the excitation signal. The round trip time-of-flight $\tau(\boldsymbol{r}, \boldsymbol{p}_i)$ is defined as

$$\tau(\boldsymbol{r}, \boldsymbol{p}_i) = t_{Tx}(\boldsymbol{r}) + t_{Rx}(\boldsymbol{r}, \boldsymbol{p}_i), \quad (3)$$

where $t_{Rx}(\boldsymbol{r}, \boldsymbol{p}_i) = \|\boldsymbol{r} - \boldsymbol{p}_i\|_2 / c$ denotes the propagation delay on receive and $t_{Tx}(\boldsymbol{r})$ is the propagation delay on transmit, supposed to be independent from the location of the emitters assuming a planar wavefront in PW imaging [44] or a spherical wavefront in DW imaging [45].

Equation (2) can be compactly expressed in terms of a linear integral operator acting on the TRF $\gamma \in L_2(\Omega)$ and outputting the measurements

$$m(t) = \mathcal{H}\{\gamma\}(t), \quad (4)$$

where $\mathcal{H} : L_2(\Omega) \to L_2([0,T])^{N_{el}}$ is an operator whose i-th component is given by

$$(\mathcal{H}\{\gamma\})_i(t) = \int_{\boldsymbol{r}\in\Omega} o(\boldsymbol{p}_i, \boldsymbol{r})\, v_{pe}(t - \tau(\boldsymbol{r}, \boldsymbol{p}_i))\, \gamma(\boldsymbol{r})\, d\boldsymbol{r}. \quad (5)$$

2) Delay-and-Sum Operator: Starting from the measurements $m(t)$, standard US image reconstruction exploits the well-known delay-and-sum (DAS) algorithm for computing the following RF image:

$$\hat{\gamma}(\boldsymbol{r}) = \sum_{i=1}^{N_{el}} a(\boldsymbol{p}_i, \boldsymbol{r})\, m_i(\tau(\boldsymbol{r}, \boldsymbol{p}_i)) \quad (6)$$

where $a(\boldsymbol{p}_i, \boldsymbol{r})$ accounts for the aperture-apodization weights, commonly applied to reduce the sidelobe levels. The intuition behind DAS is rather simple. In order to estimate the TRF at location $\boldsymbol{r}$, we sum the echo signals originating from this point and reaching the transducer elements at each given time-of-flight. Reformulating DAS in terms of a linear integral operator acting on $m(t) \in L_2([0,T])^{N_{el}}$ is also straightforward,

$$\begin{aligned}\hat{\gamma}(\boldsymbol{r}) &= \int_0^T \sum_{i=1}^{N_{el}} a(\boldsymbol{p}_i, \boldsymbol{r})\, \delta(t - \tau(\boldsymbol{r}, \boldsymbol{p}_i)) m_i(t)\, dt \\ &= \mathcal{D}\{m\}(\boldsymbol{r}), \end{aligned} \quad (7)$$

where $\mathcal{D} : L_2([0,T])^{N_{el}} \to L_2(\Omega)$.

3) Proposed Model of the Non-Stationary Blur: Based on the US propagation and DAS operators previously described, we define our model of non-stationary blur as a mapping from the TRF to the RF image given by [1]

$$\begin{aligned}\mathcal{K} &: L_2(\Omega) \to L_2(\Omega) \\ \gamma &\mapsto \hat{\gamma} = \mathcal{D}\mathcal{H}\{\gamma\}. \end{aligned} \quad (8)$$

Now, we make (8) more explicit using (2) and (6):

$$\begin{aligned}\hat{\gamma}(\boldsymbol{r}) &= \mathcal{K}\{\gamma\}(\boldsymbol{r}) \\ &\overset{(6)}{=} \sum_{i=1}^{N_{el}} a(\boldsymbol{p}_i, \boldsymbol{r})\, m_i(\tau(\boldsymbol{r}, \boldsymbol{p}_i)) \\ &\overset{(2)}{=} \int_{\boldsymbol{s}\in\Omega} \sum_{i=1}^{N_{el}} a(\boldsymbol{p}_i, \boldsymbol{r})\, o(\boldsymbol{p}_i, \boldsymbol{s})\, v_{pe}(\tau(\boldsymbol{r}, \boldsymbol{p}_i) \\ &\quad - \tau(\boldsymbol{s}, \boldsymbol{p}_i))\, \gamma(\boldsymbol{s})\, d\boldsymbol{s}. \end{aligned} \tag{9}$$

Hence, the non-stationary blur model $\mathcal{K}$, defined in (8) as the composition of the DAS and propagation operators, can also be expressed as the following Fredholm integral of the first kind, standard in shift-variant blur modeling [24],

$$\begin{aligned}\mathcal{K}&: L_2(\Omega) \to L_2(\Omega) \\ &\gamma \mapsto \int_{\boldsymbol{s}\in\Omega} \gamma(\boldsymbol{s})\, k(\cdot, \boldsymbol{s})\, d\boldsymbol{s}, \end{aligned} \tag{10}$$

where $k : \Omega \times \Omega \to \Omega$, the bivariate kernel of $\mathcal{K}$, defines the PSF and can be expressed as follows

$$k(\boldsymbol{r}, \boldsymbol{s}) = \sum_{i=1}^{N_{el}} a(\boldsymbol{p}_i, \boldsymbol{r})\, o(\boldsymbol{p}_i, \boldsymbol{s})\, v_{pe}(\tau(\boldsymbol{r}, \boldsymbol{p}_i) - \tau(\boldsymbol{s}, \boldsymbol{p}_i)). \tag{11}$$

Interestingly, if we assume that $\gamma(\boldsymbol{r}) = \delta(\boldsymbol{r} - \boldsymbol{r}_0)$, with $\boldsymbol{r}_0 \in \Omega$, then

$$\hat{\gamma}(\boldsymbol{r}) = k(\boldsymbol{r}, \boldsymbol{r}_0), \tag{12}$$

leading to the more natural interpretation of k as the PSF, i.e. the response of the US system to a TRF composed of a single point reflector located at $\boldsymbol{r}_0$.

C. Adjoint Operator Associated With the Proposed Non-Stationary Blur

In most restoration methods, the computation of the adjoint operator $\mathcal{K}^\dagger$ is required at some point. For instance, restoration approaches that require to solve a convex optimization problem need to compute the gradient of a data-fidelity term, usually expressed using the squared ℓ_2-norm. Such a gradient is defined as $\mathcal{K}^\dagger(\mathcal{K}\gamma - m)$. At the continuous level, the adjoint of the operator $\mathcal{K}$ described in (8) can straightforwardly be expressed as the composition of the adjoint DAS and adjoint propagation operators,

$$\mathcal{K}^\dagger = \mathcal{H}^\dagger \mathcal{D}^\dagger,\ \mathcal{K}^\dagger : L_2(\Omega) \to L_2(\Omega), \tag{13}$$

with,

$$\begin{aligned}\mathcal{H}^\dagger &: L_2([0,T])^{N_{el}} \to L_2(\Omega), \\ \mathcal{D}^\dagger &: L_2(\Omega) \to L_2([0,T])^{N_{el}}. \end{aligned}$$

In addition, the adjoint operators $\mathcal{D}^\dagger$ and $\mathcal{H}^\dagger$ are directly obtained from their definitions,

$$\langle \gamma, \mathcal{H}^\dagger m\rangle_{L_2(\Omega)} = \langle \mathcal{H}\gamma, m\rangle_{L_2([0,T])^{N_{el}}}, \tag{14}$$

$$\langle \gamma, \mathcal{D}m\rangle_{L_2(\Omega)} = \langle \mathcal{D}^\dagger\gamma, m\rangle_{L_2([0,T])^{N_{el}}}, \tag{15}$$

by simply flipping the order of integration over Ω and $[0, T]$ [37]. These changes are legitimate thanks to the square integrability of the involved functions.

Consequently, the adjoint operator of the propagation model is given by

$$\mathcal{H}^\dagger\{m\}(\boldsymbol{r}) = \sum_{i=1}^{N_{el}} \int_0^T o(\boldsymbol{p}_i, \boldsymbol{r})\, m_i(t)\, v_{pe}(t - \tau(\boldsymbol{r}, \boldsymbol{p}_i))\, dt, \tag{16}$$

and the adjoint DAS operator by

$$\begin{aligned}\left(\mathcal{D}^\dagger\{\gamma\}\right)_i(t) &= \int_{\boldsymbol{r}\in\Omega} a(\boldsymbol{p}_i, \boldsymbol{r})\delta(t - \tau(\boldsymbol{r}, \boldsymbol{p}_i))\gamma(\boldsymbol{r})d\boldsymbol{r}, \\ &\quad i = 1, \ldots, N_{el}. \end{aligned} \tag{17}$$

Interestingly, using the same reasoning as for $\mathcal{K}$, we show that $\mathcal{K}^\dagger$ can also be expressed using the PSF kernel defined in (11), by flipping the two arguments, i.e. using a symmetrised kernel $\tilde{k}(\boldsymbol{r}, \boldsymbol{s}) = k(\boldsymbol{s}, \boldsymbol{r})$, such that

$$\begin{aligned}\mathcal{K}^\dagger&: L_2(\Omega) \to L_2(\Omega) \\ &\gamma \mapsto \int_{\boldsymbol{s}\in\Omega} \gamma(\boldsymbol{s})\, k(\boldsymbol{s}, \cdot)\, d\boldsymbol{s}. \end{aligned} \tag{18}$$

III. Evaluation Strategy of the Proposed Model of Non-Stationary Blur

In this section, we express the non-stationary blur over a regular grid. More precisely, the TRF $\boldsymbol{\Gamma} \in \mathbb{R}^{N_x \times N_z}$ is defined on a regular grid $\Omega_\gamma = \{\boldsymbol{s}_{uv} = (x_u, z_v) \in \Omega, u = 1, \ldots, N_x, v = 1, \ldots, N_z\}$ and the RF image $\hat{\boldsymbol{\Gamma}} \in \mathbb{R}^{\hat{N}_x \times \hat{N}_z}$ is defined on a second regular grid $\Omega_{\hat{\gamma}} = \{\boldsymbol{r}_{kl} = (x_k, z_l) \in \Omega, k = 1, \ldots, \hat{N}_x, l = 1, \ldots, \hat{N}_z\}$.

A common approximation of (10) is achieved by numerical approximation of the continuous integral, leading to

$$\hat{\boldsymbol{\Gamma}} = \boldsymbol{K}\boldsymbol{\Gamma}, \tag{19}$$

where $\boldsymbol{K} : \mathbb{R}^{N_x \times N_z} \to \mathbb{R}^{\hat{N}_x \times \hat{N}_z}$, is defined element-wise by

$$\boldsymbol{K}_{kluv} = k(\boldsymbol{r}_{kl}, \boldsymbol{s}_{uv})\, \Delta_{uv}, \tag{20}$$

where Δ_{uv} is the elementary volume for the normalization of $\boldsymbol{K}$. The evaluation of (19) requires $O\left(N_x N_z \hat{N}_x \hat{N}_z N_{el}\right)$ operations, which is not computable for realistic 2D US imaging configurations where $N_x N_z$ and $\hat{N}_x \hat{N}_z$ are of the order of 10^4 to 10^6.

Many fast approximation strategies of non-stationary blur models of the form (10) have been described in the literature and briefly reviewed in Section I (See [24] for an exhaustive review of such methods). In this section, we present an alternative approach based on the specific property of the non-stationary blur in US imaging, i.e. its decomposition in terms of the propagation and DAS operators. With an appropriate discretization of the different spaces involved in the computation of such operators, we show that (10) can be efficiently approximated, while its evaluation can be performed with drastically reduced complexity compared to (19).

A. Proposed Evaluation Strategy of the Non-Stationary Blur

As for the continuous model of the blur $\mathcal{K}$, the operator $\boldsymbol{K}$ defined in (19) can be decomposed as follows

$$\boldsymbol{K} = \boldsymbol{D}_d \boldsymbol{H}_d, \tag{21}$$

where $\boldsymbol{H}_d : \mathbb{R}^{N_x \times N_z} \rightarrow L_2([0,T])^{N_{el}}$ and $\boldsymbol{D}_d : L_2([0,T])^{N_{el}} \rightarrow \mathbb{R}^{\hat{N}_x \times \hat{N}_z}$ are the partly discretized propagation and DAS operators. More precisely, $\boldsymbol{D}_d$ is computed by evaluating $\mathcal{D}$ on the regular grid $\Omega_{\hat{\gamma}}$ and $\boldsymbol{H}_d$ is computed element-wise by numerical approximation of the continuous integral involved in (5) on the regular grid Ω_γ.

As is, the operators $\boldsymbol{D}_d$ and $\boldsymbol{H}_d$ are qualified as "partly" discretized since they involve as domain and codomain, respectively, the space $L_2\left([0,T]\right)^{N_{el}}$. Such a space, while suitable for mathematical characterization of the operators is not practical in terms of computations since we cannot evaluate $\boldsymbol{D}_d$ and $\boldsymbol{H}_d$. Hence the sequential split assumption is not useful for evaluation purpose and one would still rely on (19) to compute $\boldsymbol{K\Gamma}$.

In order to benefit from the sequential split assumption, we propose to discretize the time dimension of the element-raw data such that the continuous space $[0,T]$ is approximated by N_t uniformly spaced time instants, with corresponding sampling frequency f_s. Such an assumption is particularly suited to US imaging due to the bandpass signal properties of the element-raw data, which can be accurately reconstructed from uniform samples acquired at the Nyquist rate (or using bandpass sampling). Hence, an appropriate discretization of the element-raw data space may result in an accurate approximation of the non-stationary blur. In addition, performing the discretization of the element-raw data is aligned with most recent US imaging systems which operate on digitized element-raw data.

Mathematically, we define the discrete element-raw data as the 2D matrix $\boldsymbol{M} \in \mathbb{R}^{N_t \times N_{el}}$, where each element is given by

$$\boldsymbol{M}_{ki} = m_i(t_k),\ i = 1, \ldots, N_{el},\ k = 1, \ldots, N_t, \tag{22}$$

where $t_k = (k-1)/f_s$.

Exploiting this discrete formulation, we express the blur-model as follows

$$\boldsymbol{K} = \boldsymbol{D}\boldsymbol{H}, \tag{23}$$

where $\boldsymbol{D} : \mathbb{R}^{N_t \times N_{el}} \rightarrow \mathbb{R}^{\hat{N}_x \times \hat{N}_z}$ is the discretized DAS operator and $\boldsymbol{H} : \mathbb{R}^{N_x \times N_z} \rightarrow \mathbb{R}^{N_t \times N_{el}}$ is the discretized propagation operator. The adjoint operator can be straightforwardly deduced from $\boldsymbol{K}$ as

$$\boldsymbol{K}^\dagger = \boldsymbol{H}^\dagger \boldsymbol{D}^\dagger. \tag{24}$$

With this simple discretization of the latent element-raw data space, we benefit from very efficient matrix-free implementations of the discretized propagation operator $\boldsymbol{H}$ and DAS operator $\boldsymbol{D}$ that have been developed in our previous work [37] and are expressed with more details below. In the remainder of the paper and without loss of generality, we assume that $\hat{N}_x = N_x$ and $\hat{N}_z = N_z$.

1) Fast Propagation Operator and Its Adjoint: The i-th component of the integral operator defined in (5) can be reformulated as the following convolution,

$$\left(\mathcal{H}\{\gamma\}\right)_i(t) = v_{pe} *_t \mathcal{G}_i\{\gamma\}(t), \tag{25}$$

where $*_t$ denotes the analytical convolution over the time dimension and $\mathcal{G}_i : L_2(\Omega) \rightarrow L_2([0,T])$ is defined by

$$\mathcal{G}_i\{\gamma\}(t) = \int_{\boldsymbol{r}\in\Omega} o\left(\boldsymbol{p}_i, \boldsymbol{r}\right) \gamma(\boldsymbol{r}) \delta(t - \tau(\boldsymbol{r}, \boldsymbol{p}_i)) d\boldsymbol{r}. \tag{26}$$

Alternatively, $\mathcal{G}_i\{\gamma\}(t)$ can be expressed as

$$\mathcal{G}_i\{\gamma\}(t) = \int_{\boldsymbol{r}\in\Omega} o\left(\boldsymbol{p}_i, \boldsymbol{r}\right) \gamma(\boldsymbol{r}) \delta(g_i\left(t, \boldsymbol{r}\right)) \, d\boldsymbol{r}, \tag{27}$$

where $g_i(t, \boldsymbol{r}) = t - \tau(\boldsymbol{r}, \boldsymbol{p}_i)$.

Using the co-area formula, (27) can be re-written as the following line integral [37],

$$\mathcal{G}_i\{\gamma\}(t) = \int_{\boldsymbol{r}\in S_i(t)} \frac{o\left(\boldsymbol{p}_i, \boldsymbol{r}\right) \gamma\left(\boldsymbol{r}\right)}{\mid \nabla_{\boldsymbol{r}} g_i(t, \boldsymbol{r}) \mid} d\sigma\left(\boldsymbol{r}\right), \tag{28}$$

where $S_i\left(t\right)$ is the 0-level set of the function $g_i\left(t, \boldsymbol{r}\right)$ given by

$$S_i(t) = \left\{\boldsymbol{r} \in \Omega : g_i(t, \boldsymbol{r}) = 0\right\}. \tag{29}$$

By an appropriate reparameterization of $S_i\left(t\right)$ described in our previous work [37], [38], (28) can be expressed as

$$\mathcal{G}_i\{\gamma\}(t) = \int_{\alpha\in\mathbb{R}} \frac{o\left(\boldsymbol{p}_i, \boldsymbol{r}\left(\alpha, \boldsymbol{p}_i, t\right)\right) \gamma\left(\boldsymbol{r}\left(\alpha, \boldsymbol{p}_i, t\right)\right)}{\mid \nabla_{\boldsymbol{r}} g_i(t, \boldsymbol{r}\left(\alpha, \boldsymbol{p}_i, t\right)) \mid} |J_{\boldsymbol{r}}| d\alpha, \tag{30}$$

where $\boldsymbol{r}\left(\alpha, \boldsymbol{p}_i, t\right) = \left[\alpha, z\left(\alpha, \boldsymbol{p}_i, t\right)\right]^\top$ and $|J_{\boldsymbol{r}}| : \mathbb{R}^2 \rightarrow \mathbb{R}$ denotes the Jacobian associated with the change of variable.

The numerical approximation of the integral over α leads to

$$\left(\mathcal{H}\{\gamma\}\right)_i(t) \approx \left[v_{pe} *_t \left(\sum_{j=1}^{N_x} w_j\left(\boldsymbol{p}_i, \cdot\right) \gamma\left(\boldsymbol{r}\left(\alpha_j, \boldsymbol{p}_i, \cdot\right)\right)\right)\right](t), \tag{31}$$

where $w_j\left(\boldsymbol{p}_i, t\right)$ accounts for the spatial directivity, the decay of the reflected wave, the Jacobian, the gradient of g_i and the weights related to the numerical approximation of the integral.

Discretizing (31) with respect to t leads to

$$\left(\boldsymbol{H\Gamma}\right)_{li} \approx \left(\boldsymbol{V}_{pe} \hat{\boldsymbol{m}}_i\right)_l,\ l = 1, \ldots, N_t, \tag{32}$$

where $\boldsymbol{V}_{pe} \in \mathbb{R}^{N_t \times N_t}$ is the Toeplitz matrix associated with the discrete convolution with $\boldsymbol{v}_{pe} \in \mathbb{R}^{N_t}$ and $\hat{\boldsymbol{m}}_i \in \mathbb{R}^{N_t}$ is defined element-wise as

$$\hat{\boldsymbol{m}}_i\left(t_l\right) = \sum_{j=1}^{N_x} w_j\left(\boldsymbol{p}_i, t_l\right) \gamma\left(\boldsymbol{r}\left(\alpha_j, \boldsymbol{p}_i, t_l\right)\right). \tag{33}$$

It can be noticed that (32) approximates the continuous convolution in (31) by its discrete counterpart which is crucial in the acceleration of the forward operator. Without loss of generality, we consider a "half-padded" convolution [46] with zero-padding at the boundary which explains why $\boldsymbol{V}_{pe}$ is a square matrix. "Fully-padded" and "non-padded" convolutions as well as alternative boundary methods may also be considered. Since we work on a discrete grid Ω_γ, we have to introduce N_x interpolation operators $\boldsymbol{I}_j : \mathbb{R}^{N_z} \rightarrow \mathbb{R}^{N_t \times N_{el}}$ such that

$$\gamma\left(\boldsymbol{r}\left(\alpha_j, \boldsymbol{p}_i, t_l\right)\right) \approx \left(\boldsymbol{I}_j \boldsymbol{\Gamma}_{\bullet j}\right)_{li},\ j = 1, \ldots, N_x. \tag{34}$$

We can now approximate (33) as

$$\hat{\boldsymbol{m}}_i\left(t_l\right) \approx \sum_{j=1}^{N_x} w_j\left(\boldsymbol{p}_i, t_l\right)\left(\boldsymbol{I}_j \boldsymbol{\Gamma}_{\bullet j}\right)_{li}. \tag{35}$$

Consequently, the application of the discretized forward operator $\boldsymbol{H}$ over the TRF image can be formulated as

$$\boldsymbol{H}\boldsymbol{\Gamma} = \boldsymbol{V}_{pe}\left[\sum_{j=1}^{N_x} \boldsymbol{W}_j \circ \boldsymbol{I}_j \boldsymbol{\Gamma}_{\bullet j}\right] \in \mathbb{R}^{N_t \times N_{el}}, \tag{36}$$

where $\boldsymbol{W}_j \in \mathbb{R}^{N_t \times N_{el}}$ is defined element-wise as $\left(\boldsymbol{W}_j\right)_{li} = w_j\left(\boldsymbol{p}_i, t_l\right)$.

More practically, the action of the discretized forward operator defined inside the sum in (36) can be described as a sequential application of

1) a masking operation which selects the sub-region of $\boldsymbol{\Gamma}_{\bullet j}$, $j = 1, \ldots, N_x$, that interpolates the points $\left\{\gamma\left(\boldsymbol{r}\left(\alpha_j, \boldsymbol{p}_i, t_l\right)\right)\right\}_{l,i=1}^{N_t, N_{el}}$;
2) a point-wise multiplication with the weighting matrix $\boldsymbol{W}_j$;
3) a convolution with the pulse-echo waveform.

Thus, one can see the analogy with sectional methods in the context of spatially-varying blur modeling. The main difference is that the mask does not aim to isolate regions where different stationary blurs are applied. It rather selects sub-regions where the convolutions with the pulse-echo waveform have to be applied depending on US propagation and acquisition settings (which define the parametric curves). Then, the same convolution with the pulse-echo waveform is performed in every sub-region. The adjoint operator $\mathcal{H}^\dagger$ defined in (16) can be seen as the following operation,

$$\mathcal{H}^\dagger\{m\}\left(\boldsymbol{r}\right) = \sum_{i=1}^{N_{el}} o\left(\boldsymbol{p}_i, \boldsymbol{r}\right)\left(u_{pe} *_t m_i\right)\left(\tau\left(\boldsymbol{r}, \boldsymbol{p}_i\right)\right), \tag{37}$$

where $u_{pe}\left(t\right) = v_{pe}\left(-t\right)$ is the matched filter of the pulse-echo waveform.

We introduce the convolved raw data $\tilde{m}_i = u_{pe} *_t m_i$, for $i = 1, \ldots, N_{el}$, such that

$$\mathcal{H}^\dagger\{m\}\left(\boldsymbol{r}_{sq}\right) = \sum_{i=1}^{N_{el}} o\left(\boldsymbol{p}_i, \boldsymbol{r}_{sq}\right)\tilde{m}_i\left(\tau\left(\boldsymbol{r}_{sq}, \boldsymbol{p}_i\right)\right), \tag{38}$$

for $\boldsymbol{r}_{sq} = \left(x_s, z_q\right) \in \Omega_{\hat{\gamma}}$, $s = 1, \ldots, N_x$, $q = 1, \ldots, N_z$.

The discretization of (38) with respect to t is achieved into two steps. The first one approximates the convolved raw data $\tilde{m}_i$ with its discrete counterpart as

$$\tilde{\boldsymbol{M}}_{\bullet i} = \boldsymbol{V}_{pe}^\top \boldsymbol{M}_{\bullet i}. \tag{39}$$

To complete the discretization, we introduce N_{el} interpolation operators $\boldsymbol{I}_i' : \mathbb{R}^{N_t} \to \mathbb{R}^{N_x \times N_z}$ such that

$$\tilde{m}_i\left(\tau\left(\boldsymbol{r}_{sq}, \boldsymbol{p}_i\right)\right) \approx \left(\boldsymbol{I}_i' \tilde{\boldsymbol{M}}_{\bullet i}\right)_{sq},\ i = 1, \ldots, N_{el}, \tag{40}$$

and (38) is approximated as

$$\left(\boldsymbol{H}^\dagger \boldsymbol{M}\right)_{sq} = \sum_{i=1}^{N_{el}} o\left(\boldsymbol{p}_i, \boldsymbol{r}_{sq}\right)\left(\boldsymbol{I}_i' \tilde{\boldsymbol{M}}_{\bullet i}\right)_{sq} \in \mathbb{R}. \tag{41}$$

The adjoint propagation operator $\boldsymbol{H}^\dagger$ expressed over the grid is therefore given by,

$$\boldsymbol{H}^\dagger \boldsymbol{M} = \sum_{i=1}^{N_{el}} \boldsymbol{O}_i \circ \boldsymbol{I}_i'\left(\boldsymbol{V}_{pe}^\top \boldsymbol{M}_{\bullet i}\right) \in \mathbb{R}^{N_x \times N_z}, \tag{42}$$

where $\boldsymbol{O}_i \in \mathbb{R}^{N_x \times N_z}$ is defined element-wise as $\left(\boldsymbol{O}_i\right)_{sq} = o\left(\boldsymbol{p}_i, \boldsymbol{r}_{sq}\right)$.

Similarly to the forward operator, the action of the discretized adjoint operator defined inside the sum in (42) can be seen as the application of:

1) a convolution of $\boldsymbol{M}_{\bullet i}$ with the matched filter of the pulse-echo waveform;
2) a masking operation which selects the sub-region of the $\boldsymbol{M}_{\bullet i}$ that interpolates the points $\left\{\tilde{m}_i\left(\tau\left(\boldsymbol{r}_{sq}, \boldsymbol{p}_i\right)\right)\right\}_{s,q=1}^{N_x, N_z}$;
3) a point-wise multiplication with $\boldsymbol{O}_i$.

The same remarks as for the discretized forward operator hold.

2) Fast Delay-and-Sum Operator and Its Adjoint: The DAS operator, defined in (6), can be seen as an approximation of the adjoint operator $\mathcal{H}^\dagger$ under the following assumptions:

- The pulse-echo waveform is a Dirac delta, i.e. $v_{pe}\left(t\right) = \delta\left(t\right)$;
- the aperture-apodization weights replace the spatial directivity and the radial decay $1/\boldsymbol{r}$ of the reflected wave.

Thus, the application of the discretized DAS operator on the grid is directly defined by the interpolation operation introduced in (42) as

$$\boldsymbol{D}\boldsymbol{M} = \sum_{i=1}^{N_{el}} \boldsymbol{A}_i \circ \boldsymbol{I}_i' \boldsymbol{M}_{\bullet i} \in \mathbb{R}^{N_x \times N_z}, \tag{43}$$

where $\boldsymbol{A}_i \in \mathbb{R}^{N_x \times N_z}$ is defined element-wise as $\left(\boldsymbol{A}_i\right)_{sq} = a\left(\boldsymbol{p}_i, \boldsymbol{r}_{sq}\right)$.

The application of the discretized adjoint DAS operator $\boldsymbol{D}^\dagger$ expressed over the grid can be deduced from (36) as

$$\boldsymbol{D}^\dagger \boldsymbol{\Gamma} = \sum_{j=1}^{N_x} \boldsymbol{W}_j \circ \boldsymbol{I}_j \boldsymbol{\Gamma}_{\bullet j} \in \mathbb{R}^{N_t \times N_{el}}, \tag{44}$$

where the apodization weights are used in the computation of $\boldsymbol{W}_j$.

B. Computational Complexity of the Proposed Evaluation Strategy

As already mentioned, the evaluation of $\boldsymbol{K} : \mathbb{R}^{N_x \times N_z} \to \mathbb{R}^{N_x \times N_z}$ defined in (19) requires *a priori* $O\left(\left(N_x N_z\right)^2 N_{el}\right)$ operations using (11). Such a complexity prevents its use in realistic imaging cases, where $N_x N_z$ ranges between 10^4 and 10^6 and N_{el} is few hundreds.

To solve the above limitation, the proposed evaluation strategy decomposes the computation of $\boldsymbol{K\Gamma}$ as follows:

$$\boldsymbol{K\Gamma} = \boldsymbol{D}\left(\boldsymbol{H\Gamma}\right), \tag{45}$$

where $\boldsymbol{H\Gamma}$ is first performed, generating a pseudo raw data $\boldsymbol{M}$, followed by the application of the DAS $\boldsymbol{DM}$.

The computation of $\boldsymbol{H\Gamma}$ requires to perform the following operations:

1) N_x interpolations $\boldsymbol{I}_j\boldsymbol{\Gamma}_{\bullet j}$ where each interpolation has a computational complexity of $O\left(LN_tN_{el}\right)$ with L the support of the interpolation kernel ($L \ll N_z$);
2) N_x point-wise multiplications with $\boldsymbol{W}_j$, each of which having a cost of $O\left(N_{el}N_t\right)$;
3) N_x convolutions with $\boldsymbol{v}_{pe}$ each of which with a complexity of $O\left(N_t \log N_t\right)$.

The overall computational complexity of $\boldsymbol{H\Gamma}$ is therefore:

$$\begin{aligned}\text{Cost}\left(\boldsymbol{H\Gamma}\right) &= O\left(LN_xN_{el}N_t + N_xN_{el}N_t + N_xN_t \log N_t\right)\\ &= O\left(N_xN_{el}N_t\right), \end{aligned}\tag{46}$$

since $\log N_t \ll N_{el}$ and $L \ll N_{el}$ in US imaging.

The computation of $\boldsymbol{DM}$ necessitates rather similar operations as the ones described above, apart from the convolution:

1) N_{el} interpolations $\boldsymbol{I}'_i\boldsymbol{M}_{\bullet i}$ where each interpolation has a computational complexity of $O\left(L'N_xN_z\right)$ with L' the support of the interpolation kernel ($L' \ll N_t$);
2) N_{el} point-wise multiplications with $\boldsymbol{A}_i$, each of which having a cost of $O\left(N_xN_z\right)$.

The computational complexity of $\boldsymbol{DM}$ is:

$$\text{Cost}\left(\boldsymbol{DM}\right) = O\left(L'N_{el}N_xN_z + N_{el}N_xN_z\right) \tag{47}$$

$$= O\left(N_{el}N_xN_z\right). \tag{48}$$

The overall complexity of the operation $\boldsymbol{K\Gamma}$ can be easily deduced from (46) and (48) as:

$$\text{Cost}\left(\boldsymbol{K\Gamma}\right) = O\left(N_{el}N_x\left(N_t + N_z\right)\right) \tag{49}$$

$$\approx O\left(N_{el}N_xN_z\right), \tag{50}$$

since $N_t \approx N_z$ in standard US imaging configurations. Thus we have the following:

$$\text{Cost}\left(\boldsymbol{K\Gamma}\right) \ll O((N_xN_z)^2N_{el}). \tag{51}$$

An equivalent reasoning for the computation of the adjoint operation $\boldsymbol{K}^\dagger\hat{\boldsymbol{\Gamma}}$ leads to the same computational complexity as for the forward operation. Indeed, the only difference between the two computations resides in the convolution which is negligible in the computational cost.

Thus, the proposed decomposition results in a significant decrease of the computational complexity from quadratic to linear with respect to the number of grid points N_xN_z.

Compared to the common approximation strategies of the shift-variant blur we can draw the following conclusions. If we assume that shift-variant blurs have been stored as matrices of size $N_x^b \times N_z^b$, where $N_z^b < N_z$ and $N_x^b < N_x$ (as it is often the case), their evaluations would require $O\left(N_xN_z \log N_xN_z\right)$ computations using a Fourier-domain approach or $O\left(N_x^bN_z^bN_xN_z\right)$ otherwise.

TABLE I
PROBE CHARACTERISTICS

	Diverging wave P4-2v	Plane wave L11-4v	Plane wave L12-5 50 mm
Element number	64	128	128
Center frequency	2.7 MHz	5.133 MHz	7.8 MHz
Sampling frequency	10.8 MHz	20.832 MHz	31.2 MHz
Element width	255 µm	270 µm	Unknown
Pitch	280 µm	300 µm	195 µm
Elevation focus	60 mm	20 mm	Unknown

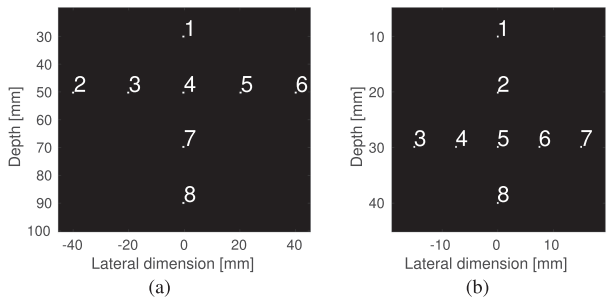

Fig. 3. Numerical point-reflector phantoms used for (a) diverging wave and (b) plane wave imaging configurations.

Using the Fourier-domain approach, the complexity is usually slightly lower than the proposed approach since $\log N_xN_z < N_{el}$ but the method does not scale as well as the proposed approach with respect to the grid size. Otherwise, the complexity highly depends on the size of the blur matrix while the complexity of the proposed approach remains linear with respect to the grid size.

IV. EXPERIMENTS

This section describes the imaging configurations, for both DW and PW imaging, used to evaluate the proposed non-stationary PSF estimation against state-of-the-art methods. It also describes the ℓ_p-based image restoration method.

A. Diverging-Wave Imaging Configuration

A simulated experiment is performed with a standard phased-array probe (P4-2v) whose characteristics are given in Table I. A single DW (2.5 MHz, 1-cycle excitation) is transmitted with a corresponding virtual point source located at z_n equal to -2.9 mm and laterally centered. No apodization is used on transmit.

The data are acquired on a numerical point-reflector phantom with eight reflectors with unit amplitude and located at positions described on Fig. 3(a). The simulation software used for this experiment is Field II [43].

B. Plane-Wave Imaging Configurations

Two standard linear-array probes are used, namely the L11-4v and the L12-5 50 mm, whose characteristics are given in Table I.

The L11-4v is used in two simulated configurations (using Field II) for which a single PW (5.208 MHz, 2.5-cycle excitation) with normal incidence is transmitted without apodization:

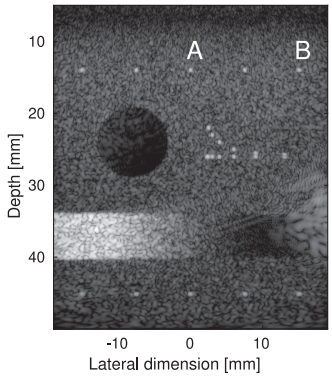

Fig. 4. Log-compressed B-mode image of the PICMUS numerical phantom. The points labeled "A" and "B" are used in Section V-B.

- A point-reflector phantom with reflectors described in Fig. 3(b);
- the PICMUS numerical phantom,[1] whose example B-mode image is displayed in Fig. 4.

The L12-5 50 mm is used to acquire *in vivo* measurements of two carotids on a Verasonics Vantage 256 system (Redmond, WA, USA). A single PW (5 MHz, 1-cycle excitation) with normal incidence is transmitted without apodization.

C. Proposed ℓ_p-Based Restoration Method

We use a ℓ_p-norm minimization, one of the most recent methods introduced in US image restoration [1], [6], [12], [19], [20], [22]. Since the discretized PSF operator has been described as a tensor in Section III-A, we have to introduce the reshaping operator $\boldsymbol{P} : \mathbb{R}^{N_x \times N_z} \rightarrow \mathbb{R}^{N_x N_z}$, such that $\boldsymbol{\gamma} = \boldsymbol{P\Gamma} \in \mathbb{R}^{N_x N_z}$. We are therefore interested in solving the following optimization problem,

$$\min_{\tilde{\boldsymbol{\gamma}} \in \mathbb{R}^{N_x N_z}} \lambda \left\| \tilde{\boldsymbol{\gamma}} \right\|_p^p + \frac{1}{2} \left\| \hat{\boldsymbol{\gamma}} - \tilde{\boldsymbol{K}} \tilde{\boldsymbol{\gamma}} \right\|_2^2, \tag{52}$$

where $\tilde{\boldsymbol{K}} = \boldsymbol{PKP}^{\dagger} \in \mathbb{R}^{N_x N_z \times N_x N_z}$ accounts for the discretized PSF operator and $\hat{\boldsymbol{\gamma}} = \boldsymbol{P}\hat{\boldsymbol{\Gamma}} \in \mathbb{R}^{N_x N_z}$, where $\hat{\boldsymbol{\Gamma}}$ is the RF image acquired by the US imaging system. In the objective function minimized in (52), the first term is the prior, the second term is the data-fidelity, $\lambda \in \mathbb{R}_+$ is a regularization parameter and p is a real so that $1 \leq p \leq 2$ [47].

The values of p are set to 1, $4/3$ or $3/2$, depending on the experiment, similar to the values used in [6] since their corresponding proximity operator are analytically defined (see appendix). The optimization algorithm used to solve the restoration problem is the fast iterative shrinkage thresholding algorithm (FISTA) described in the appendix [48].

Three different PSF estimation techniques are compared:

- The proposed non-stationary PSF;
- a stationary PSF estimated from the data using the method described in [11], denoted as stationary PSF 1;
- a stationary PSF previously simulated on Field II using a phantom made of a single scatterer located at 25 mm for PW imaging and 45 mm for DW imaging, denoted as stationary PSF 2.

The restoration is performed on RF images, obtained by applying the DAS operator on the element-raw data. The image grid spacing is set to one third of the wavelength in the lateral direction and one eighth of the wavelength in the axial direction. The apodization used on receive is the element-directivity according to Selfridge *et al.* [42].

TABLE II
COMPARISON OF THE METHODS ON THE POINT-REFLECTOR PHANTOM IN THE DIVERGING WAVE EXPERIMENT

	Method	1	2	3	4	5	6	7	8
Lat. Res [mm]	Prop. PSF	**0.32**	**0.19**	0.21	**0.50**	0.21	**0.21**	**0.60**	**0.60**
	Stat. PSF 1	0.90	0.21	**0.19**	1.4	**0.19**	**0.21**	2.2	2.7
	Stat. PSF 2	6.9	9.5	9.5	2.9	9.5	9.5	1.6	3.2
Ax. Res [mm]	Prop. PSF	0.43	0.21	0.42	0.24	**0.07**	**0.07**	0.21	0.21
	Stat. PSF 1	**0.28**	**0.07**	**0.08**	**0.08**	0.41	0.08	**0.08**	**0.08**
	Stat. PSF 2	0.46	3.6	3.6	0.55	3.6	3.6	0.37	0.39

D. Implementation Details

The methods are implemented using MATLAB.[2] For the stationary methods, we store the PSF in a matrix form and we compute the shift-invariant convolutions using the Fourier domain approach. For the proposed non-stationary blur, we implement a parallelized matrix-free evaluation of the different operators as described in [37].

Concerning FISTA, we consider a maximum number of 100 iterations and we set a stopping criterion if the relative evolution of the solution between two consecutive iterations is lower than 10^{-3}. The regularization parameter λ is empirically tuned for each method and each experiment. Automatic optimization of such a parameter is left for future work.

V. Results and Discussion

A. Point-Reflector Experiment

For these experiments, the ℓ_p-based restoration is tested with a value of p equal to 1 since we are dealing with sparse images. The comparison is based on the axial and lateral resolution, calculated as the full-width-at-half maximum (FWHM) [49] computed on the log-compressed B-mode image. The regularization parameter is empirically set to its highest value so that all the point reflectors are visible, if possible.

Table II reports the lateral and axial resolution values for the DW configuration described in Fig. 3(a). We can see that the proposed method outperforms the models based on a stationary PSF on the lateral resolution especially. This makes sense since the diffraction effect is important in DW imaging configurations resulting in significant variability in the lateral dimension. Regarding the axial resolution, it is relatively stationary along the imaging plane and the proposed method does not significantly outperform the stationary models. Fig. 5 shows the B-mode images of the point reflectors for standard DAS beamforming (top

[1][Online]. Available: https://www.creatis.insa-lyon.fr/EvaluationPlatform/picmus/index.html

[2][Online]. Available: https://github.com/LTS5/us-non-stationary-deconv

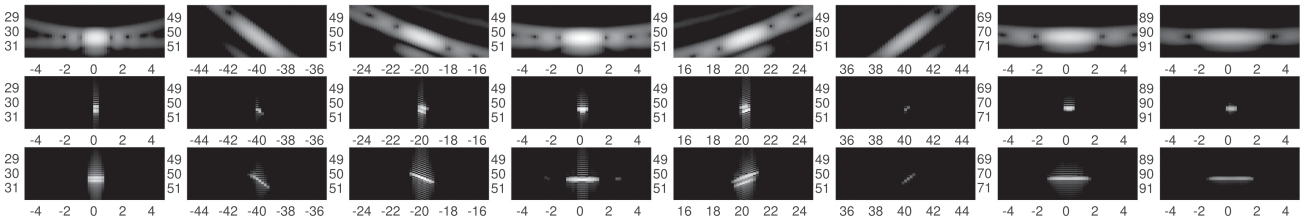

Fig. 5. Close-up of log-compressed (40 dB dynamic range) B-mode images of point-reflector 1 to point-reflector 8 (from left to right) of the DW configuration (Fig. 3(a)) obtained with standard DAS beamforming (top row), restoration with the proposed method (middle row) and restoration with the stationary PSF 1 (bottom row).

TABLE III
COMPARISON OF THE METHODS ON THE POINT-REFLECTOR PHANTOM IN THE PLANE WAVE EXPERIMENT

	Method	1	2	3	4	5	6	7	8
Lat. Res [mm]	Prop. PSF	**0.11**	**0.11**	0.11	**0.11**	**0.11**	**0.11**	**0.10**	**0.11**
	Stat. PSF 1	**0.11**	0.12	0.11	**0.11**	0.12	0.15	0.13	0.12
	Stat. PSF 2	**0.11**	0.11	**0.10**	**0.11**	**0.11**	**0.11**	0.11	**0.11**
Ax. Res [mm]	Prop. PSF	**0.04**	0.11	**0.04**	**0.04**	**0.04**	**0.04**	**0.04**	**0.04**
	Stat. PSF 1	0.21	**0.04**	**0.04**	**0.04**	**0.04**	**0.04**	**0.04**	**0.04**
	Stat. PSF 2	**0.04**	0.22	**0.04**	0.22	0.22	0.22	**0.04**	**0.04**

row), restoration with the proposed method (middle row) and restoration with the stationary PSF 1 (bottom row). It illustrates the benefit of the proposed method compared to stationary models for image restoration in case of imaging configurations with high lateral variability.

When using the method with the stationary PSF 2, it can be noted that the values for both the axial and the lateral resolution are not satisfactory, except for point-reflectors 4, 7 and 8. This is due to the fact that the PSF used in the restoration experiment has been simulated with a point reflector centered at 45 mm, close to point-reflector 4, and that point-reflectors 7 and 8 are centered as well. The high values of the resolution that one may observe in Table II are due to the fact that several points are not reconstructed. Regarding the method with the stationary PSF 1, the results are better. This can be explained by the fact that the PSF estimation method returns a sort of "averaged PSF" over the entire image, resulting in a rather uniform value of the resolution. We can nevertheless observe a non-uniformity of the resolution with respect to depth (point-reflectors 7 and 8), which emphasizes the inability of the method to capture non-stationary blur.

In the PW experiment, it can be noticed in Table III that the proposed approach is either close to or better than the best of the methods based on a stationary PSF, which means that it represents a best compromise between lateral and axial resolution. However, the results on the lateral resolution are less striking than for the DW experiment which is justified by the reduced non-stationarity of the blur compared to the DW experiment.

Regarding the stationary PSF 2, while the lateral resolution is relatively constant along the image, the values of the axial resolution are varying significantly. This is due to our choice of the regularization parameter. Indeed, it is set so that all the point reflectors are visible. When the regularization parameter is too high, the first point reflectors that vanish are point-reflectors 3 and 7 since they are the ones with the highest mismatch with the centered PSF pattern used in the restoration.

With a close look on Tables II and III, one may highlight some non-uniformity in the values of the resolution obtained with the proposed method. This can be explained by several approximations made in the physical model of the blur:

- No three-dimensional propagation: The proposed model neglects the effects related to the three-dimensional propagation in the Field II simulation, especially the element height and the elevation focus;
- planar/spherical wavefront assumption: We assume that a planar or spherical wavefront, for PW and DW respectively, of constant amplitude propagates in the medium;
- grid mismatch induced by the discretization of the continuous propagation operator and the continuous medium.

B. PICMUS Phantom Experiment

In this experiment, we compare the methods based on the dB-contrast-to-noise ratio (CNR) and lateral and axial resolution, computed on the PICMUS phantom displayed in Fig. 4. The CNR [49] is a measure of the contrast, calculated on the normalized envelope image, i.e. on the envelope image divided by its maximum value, as follows,

$$\text{CNR} = 20\log_{10}\frac{|\mu_t - \mu_b|}{\sqrt{\frac{\sigma_t^2+\sigma_b^2}{2}}}, \tag{53}$$

where (μ_t, μ_b) and (σ_t^2, σ_b^2) are the means and the variances of the target inclusion (anechoic region in Fig. 4) and the background, respectively.

The results are reported in Table IV for the ℓ_p-based restoration, with $p = 1.3$ and 1.5, and with the proposed non-stationary PSF as well as the two stationary ones. The corresponding B-mode images are available as supplementary material of this manuscript.

In Table IV, one can see that the proposed PSF outperforms the other methods on the lateral resolution. Indeed, the variability of the PSF in the axial dimension is mainly due to variations of the pulse-echo waveform induced either by frequency-dependent attenuation or by near-field effects (due to the finite element height). In the proposed simulation, we

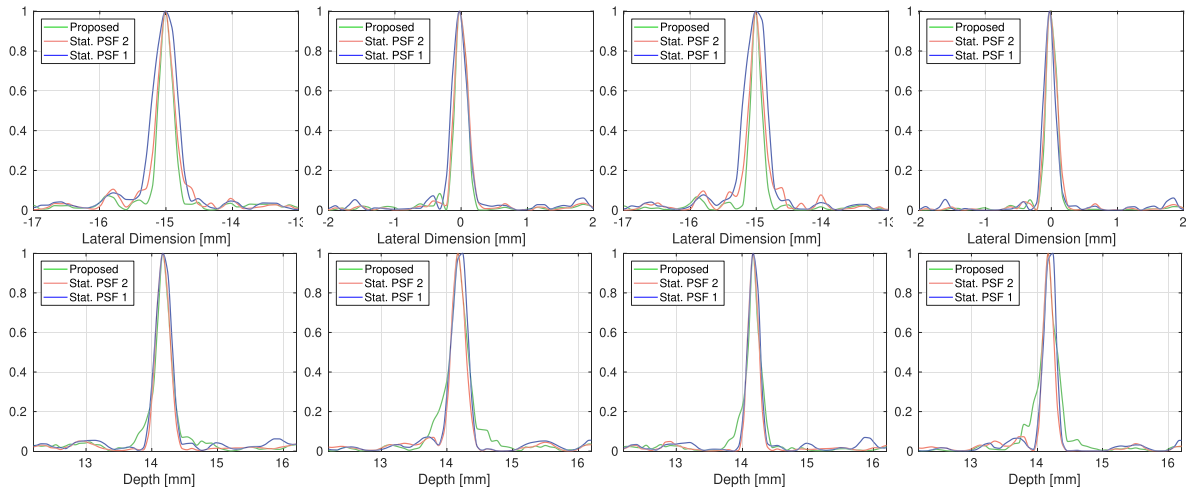

Fig. 6. x-axis (top row) and z-axis (bottom row) sections corresponding to the points A and B in Fig. 4, located at $z = 14$ mm and $x = 0$ mm and 15 mm respectively, for $p = 1.5$ (2 left plots) and $p = 1.3$ (2 right plots) and for the different blur models.

TABLE IV
COMPARISON OF THE METHODS ON THE NUMERICAL PICMUS PHANTOM

Value of p	CNR [dB]	Method	Lat. Res. [mm] 14 mm	Lat. Res. [mm] 45 mm	Ax. Res. [mm] 14 mm	Ax. Res. [mm] 45 mm
		Prop. PSF	**0.21**	**0.35**	0.24	0.28
p = 1.5	7.00	Stat. PSF 1	0.25	0.46	**0.23**	0.30
		Stat. PSF 2	0.30	0.41	0.27	**0.26**
		Prop. PSF	**0.17**	**0.25**	0.20	0.24
p = 1.3	6.00	Stat. PSF 1	0.21	0.45	**0.17**	0.22
		Stat. PSF 2	0.27	0.36	0.20	**0.18**

are at sufficiently far-field and the frequency-dependent attenuation is not taken into account. Thus, a shift-invariant model is relatively accurate.

In order to illustrate the above remarks, Fig. 6 displays the x-axis and z-axis sections corresponding to the points A and B in Fig. 4, located at $z = 14$ mm and $x = 0$ mm and 15 mm, respectively. While the effect of the proposed method is not evident on the axial dimension (bottom row), it is significant in the lateral dimension (top row).

Regarding the results of the restoration procedure, we observe that $p = 1.3$ leads to a better resolution (as can be seen in Fig. 6) but a lower contrast than $p = 1.5$. This can be explained by a close look at the definition of the CNR. Indeed, it may be deduced from (53) that the CNR favors piecewise-continuous regions where σ_b and σ_t tend to 0. On the contrary, high-resolution images exhibit a more "spiky" behaviour in the speckle region than low-resolution images which usually results in a lower mean and a higher variance, therefore in a lower CNR. In ℓ_p-based restoration, the value of p impacts the shape of the GGD prior, resulting in a variation of the resolution of the recovered TRF. The lower p, the tighter the shape of the prior, the better the resolution and the lower the CNR.

C. In Vivo Carotid Experiments

Low resolution demodulated RF images of the two carotids, obtained by DAS beamforming without restoration, are displayed on Fig. 7(a) and 7(e). The B-mode images of the ℓ_p-based restoration technique for the first carotid, and for $p = 1.5$, are displayed on Figs. 7(b), 7(c) and 7(d). The B-mode images of the ℓ_p-based restoration technique for the second carotid, and for $p = 1.3$, are displayed on Fig. 7(f), 7(g) and 7(h).

In order to quantify the benefits of the proposed model of the blur, we rely on the tissue-to-clutter ratio (TCR) [49] and the signal-to-noise ratio (SNR) [49] metrics. The TCR is a widely used measure of the contrast defined as the ratio between the average pixel intensity in a tissue region and in a background region at the same depth (to avoid bias due to time-gain compensation). Formally, it is given by

$$\mathrm{TCR} = 20 \log_{10} \left(\frac{\mu_t}{\mu_b} \right), \tag{54}$$

where μ_t and μ_b designate mean pixel intensities inside the tissue and the background regions, respectively, calculated on the normalized envelope.

The SNR is calculated as

$$\mathrm{SNR} = \frac{|\mu_t - \mu_b|}{\sqrt{\sigma_b^2 + \sigma_t^2}}, \tag{55}$$

where (μ_t, μ_b) and (σ_t, σ_b) are the mean and standard deviation of the pixel intensities of a tissue and a blood regions, respectively, calculated on a linearized image obtained from the log-compressed B-mode image. We choose a background region located inside the carotid artery and a tissue region located at the same depth, as described in Fig. 8.

TCR and SNR values, reported in Table V, demonstrate that the proposed non-stationary model outperforms stationary models for nearly all experiments. Regarding the impact of the value of p, the same trend as for the PICMUS experiment is observed, i.e. a lower value of p leads to a lower SNR induced by higher variance of the speckle pattern. In addition, visual assessment of the B-mode images displayed in Fig. 7 shows that the restoration methods all lead to a significantly higher resolution than the unprocessed B-mode image. The deblurring effect is more pronounced for the proposed method and the stationary PSF 1

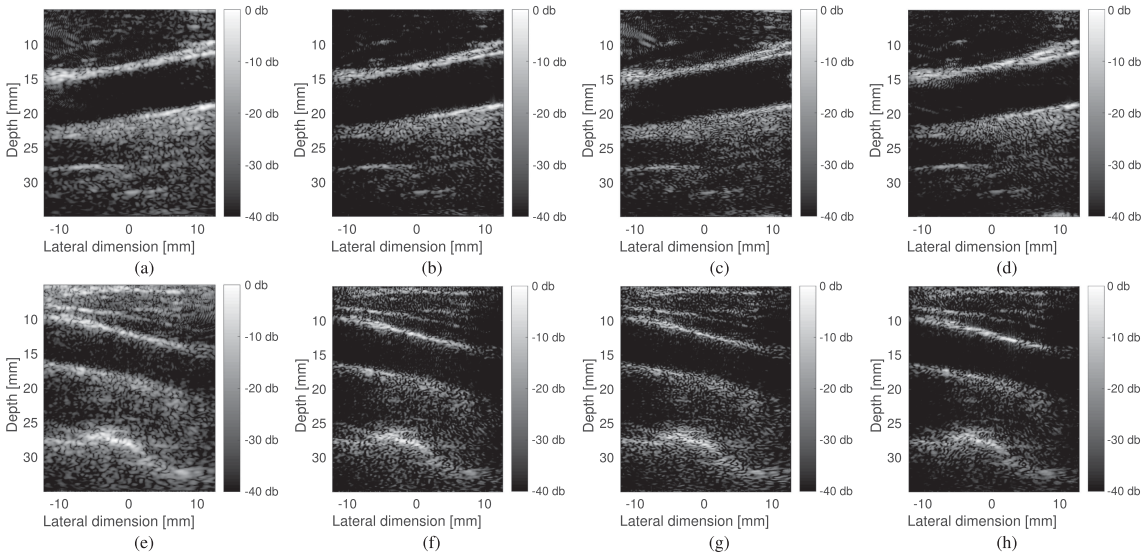

Fig. 7. (a)-Low resolution (LR) image of carotid 1; High-resolution (HR) image obtained for $p = 1.5$ with (b)-the proposed method, (c)-the stationary PSF 1 and (d)-the stationary PSF 2; (e)-LR image of carotid 2; HR image obtained for $p = 1.3$ with (f)-the proposed method, (g)-the stationary PSF 1 and (h)-the stationary PSF 2.

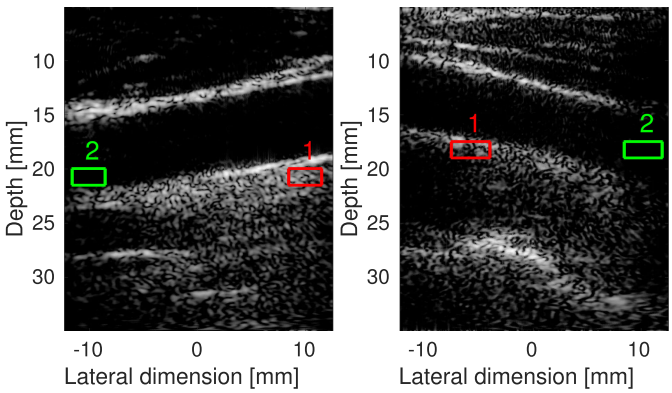

Fig. 8. Tissue (1) and blood (2) regions used for the computation of the tissue-to-clutter ratio and contrast-to-noise ratio.

TABLE V
COMPARISON OF THE METHODS ON THE IN-VIVO CAROTIDS

Value of p	Carotid number	Method	SNR [–]	TCR [dB]
p = 1.5	1	Prop. PSF	**49.1**	**29.5**
		Stat. PSF 1	27.9	26.2
		Stat. PSF 2	38.6	28.1
p = 1.3	2	Prop. PSF	21.5	**30.5**
		Stat. PSF 1	21.1	24.4
		Stat. PSF 2	**36.1**	28.4

than for the stationary PSF 2, as can be seen on the artery wall. In addition, the proposed method allows a better reconstruction of the textured area, such as the speckle region under the lower artery wall, than the methods based on a stationary PSF.

D. On Computation Times of the Proposed Strategy

In Section III-B, we have derived the computational complexity of the proposed evaluation strategy and demonstrated that it scales linearly with respect to the grid size. In this section, we discuss the practical implications of this in terms of computation times necessary to evaluate the forward blur operator.

TABLE VI
COMPUTATION TIMES OF DIFFERENT BLUR EVALUATION STRATEGIES

(N_x, N_z)	Evaluation times		
	Roquette *et al.* [1]	proposed	Stationary
(64, 100)	3.5×10^{1} s	8.8×10^{-2} s	3.7×10^{-4} s
(128, 200)	3.4×10^{2} s	1.1×10^{-1} s	6.5×10^{-4} s
(256, 200)	1.6×10^{3} s	1.9×10^{-1} s	1.2×10^{-3} s

More precisely, we consider a PW experiment with the L11-4v probe described in Table I. We compare various grid sizes characterized by the corresponding values of N_x and N_z. For each tuple (N_x, N_z), we estimate the average evaluation time of the forward blur operator over 10 runs on an Intel Core i7-4930K CPU @ 3.40 GHz equipped with MATLAB R2017A. We compare the proposed evaluation strategy, the one described by Roquette *et al.* [1] and the evaluation of a stationary blur model using the Fourier domain approach. Table VI reports the computation times of the three methods for the different grid sizes.

We can see that the proposed strategy is two orders of magnitude faster than the one developed by Roquette *et al.* even in the configuration with the smallest grid size. In addition, we observe significant differences in scaling between the two methods resulting from the difference in computational complexity.

We notice that the proposed strategy is several orders of magnitude slower than the stationary method. This is due to the fact that the Fourier-domain approach relies on fast Fourier transforms which have been highly optimized in MATLAB (built-in function) while the proposed approach entirely relies on a non-optimized MATLAB code. First implementations of the

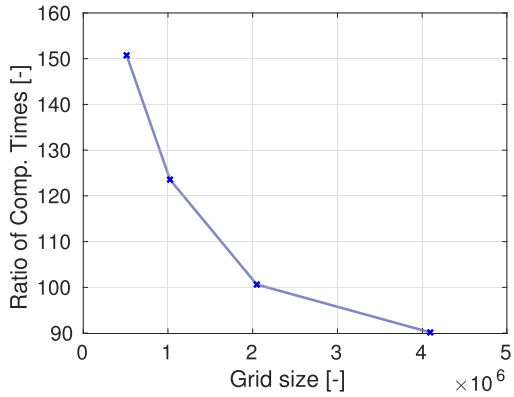

Fig. 9. Ratio of computation times between the proposed evaluation strategy and the Fourier domain evaluation of the stationary blur for varying grid sizes.

propagation and DAS operators on graphical processing units highlight the high potential for parallelizability of the proposed method [37], [38].

In addition, Fig. 9 displays ratios of evaluation times between the proposed method and the stationary model for realistic values of the grid sizes. Indeed, we fix $N_x = 512$ which corresponds to one fourth wavelength spacing and we vary N_z between 1000 and 8000.

We empirically observe that the proposed method scales better with the grid than the Fourier domain approach which corroborates the theoretical study of the complexity of Section III-B.

E. Proposed Method in the Context of Shift-Variant Deblurring Approaches

In Section III, we have shown that the model of non-stationary blur cannot be neither evaluated nor stored in realistic imaging scenarios, which is a common problem in many image restoration tasks [24].

At this stage, we may have leveraged various existing approximations of shift-variant blur, depending on the properties of the PSF field, e.g. dimensionality and smoothness, and solved the corresponding image restoration task. Instead, we have proposed a strategy based on a decomposition of the blur-model coupled with an appropriate discretization of the latent element-raw data space.

A legitimate question that one may wonder is to what extent existing shift-variant deblurring strategies, based on different approximations of the non-stationary blur can be compared to the proposed approach. Indeed, given the bivariate kernel $k(\boldsymbol{r}, \boldsymbol{s})$ defined in (11), it would be possible to apply shift-variant approximation methods such as sectional methods or interpolation of the PSF.

While such approaches may be computationally advantageous in some cases, their complexity does not scale as well as the proposed approach (they rely on convolutions that can be achieved in $O(N_x N_z \log(N_x N_z))$). More importantly, shift-variant approximation techniques, based on sectional methods [24]–[29] or on the interpolation of few kernels evaluated in different regions of the image [24] would be intrinsically less accurate than the proposed strategy. Indeed, the strength of the proposed approach is that it leads to an exact approximation of the blur matrix (provided a sufficiently high sampling of the time dimension which is easily feasible) while existing methods would always return an approximation of the blur matrix. It is especially the case in PW and DW imaging where the PSF is anisotropic and highly spatially varying due to diffraction effects.

Other approaches, based on column-wise or row-wise decomposition of the blur matrix $\tilde{\boldsymbol{K}}$ [23], [30] require to compute the singular value decomposition of $\tilde{\boldsymbol{K}}$, unfeasible in US imaging due to the large size of the matrix.

VI. Conclusion

In this work, we present a physical model of non-stationary blur in the context of 2D ultrasound imaging with plane-wave and diverging-wave insonifications and propose an evaluation strategy for image restoration purpose. The model is expressed as the composition of an ultrasound propagation operator which relates the tissue-reflectivity function to the measured echo signals, and a delay-and-sum operator which forms the radio-frequency image from the echo signals. We demonstrate by an explicit derivation of the operators that the proposed model can be expressed as a Fredholm integral of the first kind, standard in shift-variant blur modeling.

The evaluation strategy exploits such a decomposition at the discrete level coupled with an additional discretization of the latent element-raw data space, the latter being motivated by bandpass signal properties of echo signals in ultrasound imaging. These two aspects allow us to benefit from computationally efficient formulations of the ultrasound propagation and delay-and-sum operators, derived in previous works and based on parametric formulations of time-of-flight equations, interpolation on appropriate grids and discrete convolutions. We demonstrate theoretically that the proposed strategy scales linearly, rather than quadratically, with the number of grid points and we show its benefits in practical scenarios.

As an example application, we use the model for ultrasound image restoration with a maximum-a-posteriori estimation algorithm. We demonstrate through simulated and *in vivo* examples that the restoration approach with the proposed model can outperform recent state-of-the-art restoration methods based on stationary models of the blur.

Appendix
Fast Iterative Shrinkage Thresholding Algorithm and Proximity Operators

A. Fast Iterative Shrinkage Thresholding Algorithm

This section briefly presents the fast iterative shrinkage thresholding algorithm (FISTA) used to solve Problem (52). For an in-depth description of the method, please refer to [48]. FISTA is an accelerated version of the well-known iterative soft thresholding algorithm (ISTA), that can be used to solve the

Algorithm 1: FISTA Used to Solve Problem (56).

Require: $\boldsymbol{A}, \phi, \boldsymbol{y}, L \geq \lambda_{max}\left(\boldsymbol{A}^T\boldsymbol{A}\right)$
  initialization: $i = 1, t_0 = 1, \boldsymbol{x}_{-1} = \boldsymbol{x}_0 = \boldsymbol{0}$
  repeat
    $t_i \leftarrow \frac{1+\sqrt{1+4t_{i-1}^2}}{2}, \quad \alpha_i \leftarrow \frac{1-t_{i-1}}{t_i}$
    $\boldsymbol{c}_i \leftarrow \alpha_i \boldsymbol{x}_{i-2} + (1-\alpha_i)\,\boldsymbol{x}_{i-1}$
    $\boldsymbol{x}_i \leftarrow \text{prox}_\phi\left(\boldsymbol{c}_i + \frac{1}{L}\boldsymbol{A}^T\left(\boldsymbol{y} - \boldsymbol{A}\boldsymbol{c}_i\right); \frac{1}{L}\right)$
    $i \leftarrow i + 1$
  until stopping criterion
  return $\boldsymbol{x}_i$

following problem:

$$\min_{\boldsymbol{x}\in\mathbb{R}^N} \|\boldsymbol{y} - \boldsymbol{A}\boldsymbol{x}\|_2^2 + \phi(\boldsymbol{x}), \tag{56}$$

where $\boldsymbol{y} \in \mathbb{R}^M$, $\boldsymbol{x} \in \mathbb{R}^N$, $\boldsymbol{A} \in \mathbb{R}^{M\times N}$, $\phi : \mathbb{R}^N \to \mathbb{R}$ is a non-smooth convex regularizer.

FISTA is composed of an acceleration step and a proximal gradient step described in Algorithm 1. The proximal gradient step involves the following proximity operator [50]:

$$\text{prox}_\phi(\boldsymbol{x};\lambda) = \arg\min_{\boldsymbol{z}\in\mathbb{R}^N} \lambda\phi(\boldsymbol{z}) + \frac{1}{2}\|\boldsymbol{z} - \boldsymbol{x}\|_2^2. \tag{57}$$

In Algorithm 1, $\lambda_{max}\left(\boldsymbol{A}^T\boldsymbol{A}\right)$ denotes the highest eigenvalue of $\boldsymbol{A}^T\boldsymbol{A}$.

B. Proximity Operators Associated With the ℓ_p-norm

We consider the proximity operator defined in (57), where $\phi(\boldsymbol{x}) = \|\boldsymbol{x}\|_p^p$ and $p \geq 1$. Thanks to the separability of the two functions involved in the proximity operator, the problem can be solved element-wise. According to Table 10.2 of [50], the following equivalence holds:

$$z_i = \arg\min_{z_i\in\mathbb{R}} \lambda|z_i|^p + \frac{1}{2}(z_i - x_i)^2, \forall(x_i, z_i) \in \mathbb{R}\times\mathbb{R}, \lambda > 0 \tag{58}$$

$$\Leftrightarrow z_i = \text{sign}(x_i)\, q,\ q \geq 0,\ q + p\lambda q^{p-1} = |x_i|. \tag{59}$$

Thus, in order to derive the proximity operator associated with the ℓ_p-norm, one has to solve (59), which involves finding roots of a polynomial with arbitrarily high degree and can be achieved using Newton's method.

For specific values of p, the polynomial may have a degree lower or equal to 3. In such cases, (59) has an analytical solution. This is the case for the values of p considered in the study.

1) Case $p = 1$: The solution of (59) is immediately deduced as:

$$z_i = \text{sign}(x_i)\max(|x_i| - \lambda, 0), \tag{60}$$

which is the well-known soft-thresholding operator.

2) Case $p = 3/2$: The solution of (59) involves to find the positive root of the following polynomial of order 2:

$$0 = q + \frac{3}{2}\lambda q^{1/2} - |x_i| \tag{61}$$

$$\Leftrightarrow 0 = q^2 - \left(2|x_i| + \frac{9}{4}\lambda^2\right)q + x_i^2,\ |x_i| \geq q \tag{62}$$

$$\Leftrightarrow q = |x_i| + \frac{9}{8}\lambda\left(\lambda - \sqrt{\frac{16}{9}|x_i| + \lambda^2}\right). \tag{63}$$

3) Case $p = 4/3$: The solution of (59) involves to find the positive root of the following polynomial of order 3:

$$0 = q + \frac{4}{3}\lambda q^{1/3} - |x_i| \tag{64}$$

$$\Leftrightarrow 0 = q^3 - 3|x_i|q^2 + \left(3|x_i|^2 + \frac{64}{27}\lambda^3\right)q - |x_i|^3. \tag{65}$$

Using Cardano's method and after several calculations not detailed here, one may obtain the following value of q:

$$q = |x_i| + \frac{1}{9}\left(-\frac{16\cdot 2^{1/3}\cdot\lambda^2}{(z - 27|x_i|)^{1/3}} + 2^{5/3}\lambda\,(z - 27|x_i|)^{1/3}\right) \tag{66}$$

$$z = \sqrt{256\lambda^3 + 729|x_i|^2}. \tag{67}$$

REFERENCES

[1] L. Roquette, M. Simeoni, P. Hurley, and A. Besson, "On an analytical, spatially-varying, point-spread-function," in *Proc. IEEE Int. Ultrason. Symp.*, 2017, pp. 1–4.

[2] G. S. Alberti, H. Ammari, F. Romero, and T. Wintz, "Mathematical analysis of ultrafast ultrasound imaging," *SIAM J. Appl. Math.*, vol. 77, no. 1, pp. 1–25, Jan. 2017.

[3] W. Vollmann, "Resolution enhancement of ultrasonic B-scan images by deconvolution," *IEEE Trans. Sonics Ultrason.*, vol. SU-29, no. 2, pp. 78–82, Mar. 1982.

[4] C. N. Liu, M. Fatemi, and R. C. Waag, "Digital processing for improvement of ultrasonic abdominal images," *IEEE Trans. Med. Imag.*, vol. MI-2, no. 2, pp. 66–75, Jun. 1983.

[5] T. Loupas, S. D. Pye, and W. N. McDicken, "Deconvolution in medical ultrasonics: Practical considerations," *Phys. Med. Biol.*, vol. 34, no. 11, pp. 1691–1700, Nov. 1989.

[6] Z. Chen, A. Basarab, and D. Kouame, "Compressive deconvolution in medical ultrasound imaging," *IEEE Trans. Med. Imag.*, vol. 35, no. 3, pp. 728–737, Mar. 2016.

[7] O. V. Michailovich, "Nonstationary blind deconvolution of medical ultrasound scans," *Proc. SPIE*, vol. 10139, Mar. 2017, Art. no 101391C.

[8] U. R. Abeyratne, A. P. Petropulu, and J. M. Reid, "Higher order spectra based deconvolution of ultrasound images," *IEEE Trans. Ultrason., Ferroelect., Freq. Control*, vol. 42, no. 6, pp. 1064–1075, Nov. 1995.

[9] T. Taxt, "Comparison of cepstrum-based methods for radial blind deconvolution of ultrasound images," *IEEE Trans. Ultrason., Ferroelect., Freq. Control*, vol. 44, no. 3, pp. 666–674, May 1997.

[10] T. Taxt and J. Strand, "Two-dimensional noise-robust blind deconvolution of ultrasound images," *IEEE Trans. Ultrason., Ferroelect., Freq. Control*, vol. 48, no. 4, pp. 861–867, Jul. 2001.

[11] O. Michailovich and D. Adam, "A novel approach to the 2-D blind deconvolution problem in medical ultrasound," *IEEE Trans. Med. Imag.*, vol. 24, no. 1, pp. 86–104, Jan. 2005.

[12] M. Alessandrini *et al.*, "A restoration framework for ultrasonic tissue characterization," *IEEE Trans. Ultrason., Ferroelect., Freq. Control*, vol. 58, no. 11, pp. 2344–2360, Nov. 2011.

[13] J. Jensen, "Estimation of in vivo pulses in medical ultrasound," *Ultrason. Imag.*, vol. 16, no. 3, pp. 190–203, Jul. 1994.

[14] T. Taxt, "Radial homomorphic deconvolution of B-mode medical ultrasound images," in *Proc. 12th IAPR Int. Conf. Pattern Recognit.*, 1994, pp. 149–152.
[15] G. Demoment, R. Reynaud, and A. Herment, "Range resolution improvement by a fast deconvolution method," *Ultrason. Imag.*, vol. 6, no. 4, pp. 435–451, Oct. 1984.
[16] J. Jensen and S. Leeman, "Nonparametric estimation of ultrasound pulses," *IEEE Trans. Biomed. Eng.*, vol. 41, no. 10, pp. 929–936, Oct. 1994.
[17] R. Demirli and J. Saniie, "Model-based estimation of ultrasonic echoes. Part I: Analysis and algorithms," *IEEE Trans. Ultrason., Ferroelect., Freq. Control*, vol. 48, no. 3, pp. 787–802, May 2001.
[18] D. Iraca, L. Landini, and L. Verrazzani, "Power spectrum equalization for ultrasonic image restoration," *IEEE Trans. Ultrason., Ferroelect., Freq. Control*, vol. 36, no. 2, pp. 216–222, Mar. 1989.
[19] O. Michailovich and A. Tannenbaum, "Blind deconvolution of medical ultrasound images: A parametric inverse filtering approach," *IEEE Trans. Image Process.*, vol. 16, no. 12, pp. 3005–3019, Dec. 2007.
[20] N. Zhao, Q. Wei, A. Basarab, D. Kouame, and J.-Y. Tourneret, "Blind deconvolution of medical ultrasound images using a parametric model for the point spread function," in *Proc. IEEE Int. Ultrason. Symp.*, 2016, pp. 1–4.
[21] R. Jirik and T. Taxt, "Two-dimensional blind Bayesian deconvolution of medical ultrasound images," *IEEE Trans. Ultrason., Ferroelect., Freq. Control*, vol. 55, no. 10, pp. 2140–2153, Oct. 2008.
[22] R. Morin, S. Bidon, A. Basarab, and D. Kouame, "Semiblind deconvolution for resolution enhancement in ultrasound imaging," in *Proc. IEEE Int. Conf. Image Process.*, 2013, pp. 1413–1417.
[23] F. Sroubek, J. Kamenicky, and Y. M. Lu, "Decomposition of space-variant blur in image deconvolution," *IEEE Signal Process. Lett.*, vol. 23, no. 3, pp. 346–350, Mar. 2016.
[24] L. Denis, E. Thiébaut, F. Soulez, J. M. Becker, and R. Mourya, "Fast approximations of shift-variant blur," *Int. J. Comput. Vis.*, vol. 115, no. 3, pp. 253–278, Apr. 2015.
[25] M. Hirsch, S. Sra, B. Schölkopf, and S. Harmeling, "Efficient filter flow for space-variant multiframe blind deconvolution," in *Proc. IEEE Comput. Soc. Conf. Comput. Vis. Pattern Recognit.*, 2010, pp. 607–614.
[26] J. G. Nagy and D. P. O'Leary, "Restoring images degraded by spatially variant blur," *SIAM J. Sci. Comput.*, vol. 19, no. 4, pp. 1063–1082, Jul. 1998.
[27] C. Preza and J.-A. Conchello, "Depth-variant maximum-likelihood restoration for three-dimensional fluorescence microscopy," *J. Opt. Soc. Amer. A*, vol. 21, no. 9, pp. 1593–1601, Sep. 2004.
[28] J. Bardsley, S. Jefferies, J. Nagy, and R. Plemmons, "A computational method for the restoration of images with an unknown, spatially-varying blur," *Opt. Express*, vol. 14, no. 5, pp. 1767–1782, Mar. 2006.
[29] M. I. Florea, A. Basarab, D. Kouame, and S. A. Vorobyov, "An axially variant kernel imaging model applied to ultrasound image reconstruction," *IEEE Signal Process. Lett.*, vol. 25, no. 7, pp. 961–965, Jul. 2018.
[30] D. Miraut and J. Portilla, "Efficient shift-variant image restoration using deformable filtering (Part I)," *EURASIP J. Adv. Signal Process.*, vol. 2012, no. 1, pp. 1–20, May 2012.
[31] R. C. Flicker and F. J. Rigaut, "Anisoplanatic deconvolution of adaptive optics images." *J. Opt. Soc. Amer.*, vol. 22, no. 3, pp. 504–513, Mar. 2005.
[32] T. Hrycak, S. Das, G. Matz, and H. G. Feichtinger, "Practical estimation of rapidly varying channels for OFDM systems," *IEEE Trans. Commun.*, vol. 59, no. 11, pp. 3040–3048, Sep. 2011.
[33] P. Escande and P. Weiss, "Sparse wavelet representations of spatially varying blurring operators," *SIAM J. Imag. Sci.*, vol. 8, no. 4, pp. 2976–3014, Dec. 2015.
[34] J. Wei, C. A. Bouman, and J. P. Allebach, "Fast space-varying convolution using matrix source coding with applications to camera stray light reduction," *IEEE Trans. Image Process.*, vol. 23, no. 5, pp. 1965–1979, May 2014.
[35] H. Gomersall, D. Hodgson, R. Prager, N. Kingsbury, G. Treece, and A. Gee, "Efficient implementation of spatially-varying 3-D ultrasound deconvolution," *IEEE Trans. Ultrason., Ferroelect., Freq. Control*, vol. 58, no. 1, pp. 234–238, Jan. 2011.
[36] G. David, J.-L. Robert, B. Zhang, and A. F. Laine, "Time domain compressive beam forming of ultrasound signals," *J. Acoust. Soc. Amer.*, vol. 137, no. 5, pp. 2773–2784, May 2015.
[37] A. Besson *et al.*, "Ultrafast ultrasound imaging as an inverse problem: Matrix-free sparse image reconstruction," *IEEE Trans. Ultrason., Ferroelect., Freq. Control*, vol. 65, no. 3, pp. 339–355, Mar. 2018.
[38] A. Besson, D. Perdios, F. Martinez, M. Arditi, Y. Wiaux, and J.-P. Thiran, "USSR: An ultrasound sparse regularization framework," in *Proc. IEEE Int. Ultrason. Symp.*, 2017, pp. 1–4.
[39] M. Vetterli, J. Kovačević, and V. K. Goyal, *Foundations of Signal Processing*. Cambridge, U.K.: Cambridge Univ. Press, Sep. 2014.
[40] M. F. Schiffner and G. Schmitz, "Fast pulse-echo ultrasound imaging employing compressive sensing," in *Proc. IEEE Int. Ultrason. Symp.*, 2011, pp. 1–4.
[41] P. R. Stepanishen, "The time-dependent force and radiation impedance on a piston in a rigid infinite planar baffle," *J. Acoust. Soc. Amer.*, vol. 49, no. 1A, pp. 841–849, Jan. 1971.
[42] A. R. Selfridge, G. S. Kino, and B. T. Khuri-Yakub, "A theory for the radiation pattern of a narrow-strip acoustic transducer," *Appl. Phys. Lett.*, vol. 37, no. 1, Apr. 1980, Art. no. 35.
[43] J. Jensen and N. Svendsen, "Calculation of pressure fields from arbitrarily shaped, apodized, and excited ultrasound transducers," *IEEE Trans. Ultrason., Ferroelect., Freq. Control*, vol. 39, no. 2, pp. 262–267, Mar. 1992.
[44] G. Montaldo, M. Tanter, J. Bercoff, N. Benech, and M. Fink, "Coherent plane-wave compounding for very high frame rate ultrasonography and transient elastography," *IEEE Trans. Ultrason., Ferroelect., Freq. Control*, vol. 56, no. 3, pp. 489–506, Mar. 2009.
[45] C. Papadacci, M. Pernot, M. Couade, M. Fink, and M. Tanter, "High-contrast ultrafast imaging of the heart," *IEEE Trans. Ultrason., Ferroelect., Freq. Control*, vol. 61, no. 2, pp. 288–301, Feb. 2014.
[46] V. Dumoulin and F. Visin, "A guide to convolution arithmetic for deep learning," vol. 587, arXiv:1603.07285, Mar. 2016.
[47] O. Scherzer, H. Grossauer, F. Lenzen, M. Grasmair, and M. Haltmeier, *Variational Methods in Imaging (Applied Mathematical Sciences)*, vol. 167. New York, NY, USA: Springer, 2009.
[48] A. Beck and M. Teboulle, "A fast iterative shrinkage-thresholding algorithm for linear inverse problems," *SIAM J. Imag. Sci.*, vol. 2, no. 1, pp. 183–202, Jan. 2009.
[49] M. C. Van Wijk and J. M. Thijssen, "Performance testing of medical ultrasound equipment: Fundamental vs. harmonic mode," *Ultrasonics*, vol. 40, no. 1–8, pp. 585–591, May 2002.
[50] P. L. Combettes and J.-C. Pesquet, "Proximal splitting methods in signal processing," in *Fixed-Point Algorithms Inverse Problems in Science and Engineering*, vol. 49. New York, NY, USA: Springer, 2011, pp. 185–212.

Authors' photographs and biographies not available at the time of publication.